Development of Ce^3 and Li co-doped magnesium borate glass ceramics for optically stimulated luminescence dosimetry

AUTHOR(S):

Kitagawa, Yuuki; Yukihara, Eduardo G.; Tanabe, Setsuhisa

CITATION:

Kitagawa, Yuuki ...[et al]. Development of Ce^3 and Li co-doped magnesium borate glass ceramics for optically stimulated luminescence dosimetry. Journal of Luminescence 2021, 232: 117847.

ISSUE DATE:

2021-04

URL:

http://hdl.handle.net/2433/263899

Journal of Luminescence 232 (2021) 117847

Contents lists available at ScienceDirect

Journal of Luminescence

journal homepage: http://www.elsevier.com/locate/jlumin

Development of Ce^{3+} and Li^{+} co-doped magnesium borate glass ceramics for optically stimulated luminescence dosimetry

Yuuki Kitagawa [a], Eduardo G. Yukihara [b,*], Setsuhisa Tanabe [a]

[a] Graduate School of Human and Environmental Studies, Kyoto University, Kyoto, 606-8501, Japan
[b] Department of Radiation Safety and Security, Paul Scherrer Institute, Forschungsstrasse 111, 5232, Villigen PSI, Switzerland

ARTICLE INFO

Keywords:
Glass-ceramics
Storage phosphors
Dosimeter
Optically stimulated luminescence
Cerium

ABSTRACT

Magnesium tetraborate, MgB_4O_7, is an attractive host material for dosimetry due to the two characteristics: its low effective atomic number ($Z_{eff} = 8.4$) and high neutron capture cross-section of the ^{10}B isotope. Particularly, Ce^{3+} and Li^{+} ions co-doped MgB_4O_7 has shown optically stimulated luminescence (OSL) signal comparable to that of Al_2O_3:C, which is a well-known OSL dosimetry material. In this work, for further improvement of the dosimetric properties, a new synthesis route for MgB_4O_7:Ce^{3+}-Li^{+} is described: glass-ceramic (GC) MgB_4O_7:Ce^{3+}-Li^{+} samples were prepared by heat treatment of the magnesium borate glass with the composition, $25MgO–72B_2O_3–3Li_2O$-$0.3Ce^{3+}$. The prepared GC samples show UV-blue radioluminescence assigned to the Ce^{3+} $5d \rightarrow 4f$ transition under X-ray irradiation and two thermoluminescence (TL) glow peaks related to the shallow and deep electron traps. Although fading of the TL and OSL signal was observed due to electron release from the shallow traps, the electrons captured by deep traps were stable at room temperature. Particularly, GC samples annealed at 750 °C and 800 °C, named GC750 and GC800, showed stable OSL up to 10 h following β-ray irradiation, after an initial fading mainly due to the presence of shallow traps in the material. From the viewpoint of this fading ratio, GC750 and GC800 showed potential as a practical OSL dosimeter.

1. Introduction

The fast-paced technological advances in a variety of fields which either uses ionizing radiation (X-rays, β-rays, γ-rays, neutrons, as well as accelerated particles such as protons, and other heavy ions) directly for its therapeutical or analytical properties, or which produces radiation as a by-product, or both, imposes increasing challenges for the dosimetry of such fields. Some of the most challenging aspects nowadays are the dosimetry of small fields such as those found in modern radiation therapy and radiosurgery due to the large dose gradients involved [1], the dosimetry of pulsed fields created in modern accelerators (including laser-based accelerators) due to the high instantaneous dose-rates during the pulses [2,3], and the dosimetry in the presence of magnetic fields such as in those fields found in Magnetic Resonance Imaging-Guided Radiation Therapy (MRIgRT) [4].

Dosimetry refers to the quantification of the energy deposited by ionizing radiation for purposes of radiation protection, quality assurance, and overall characterization of the radiation fields. A wide variety of active and passive dosimeters are available, but all have advantages and disadvantages for each specific application [5]. Passive detectors, while not offering real-time information, are very popular in radiation protection because of their small size, low cost, high-sensitivity, precision, and convenience. From those, luminescence detectors, such as those based on radiophotoluminescence (RPL) [6,7], thermoluminescence (TL) [8], and optically stimulated luminescence (OSL) [9,10] are among the most popular for radiation measurements. The readout of RPL and OSL detectors, in particular, is completely optical, therefore practical and suitable for the development of 2D dosimetry techniques for measurements in high dose-gradient fields [11–13]. Since the luminescence processes in these detectors are based on the electron-hole trapping/detrapping processes taking place in solid-state insulating crystalline materials in a time-scale of 10^{-15}–10^{-13} s [14], the techniques may also offer advantages such as independence on dose-rate [15] and magnetic field [16].

Fig. 1 illustrates the electron trapping-detrapping processes occurring within the luminescence detectors exposed to ionizing radiation. First, electrons in the host valence band (VB) are excited by ionizing radiation (arrow 1). Since the energy of ionizing radiation is much higher than the bandgap of host compounds, electrons in the order of 10^5 ~10^6 per MeV are generated. In the case of scintillators, electron-

* Corresponding author.
E-mail addresses: kitagawa.yuuki.66w@st.kyoto-u.ac.jp (Y. Kitagawa), Eduardo.Yukihara@psi.ch (E.G. Yukihara), tanabe.setsuhisa.4v@kyoto-u.ac.jp (S. Tanabe).

https://doi.org/10.1016/j.jlumin.2020.117847
Received 6 October 2020; Received in revised form 11 December 2020; Accepted 13 December 2020
Available online 25 December 2020

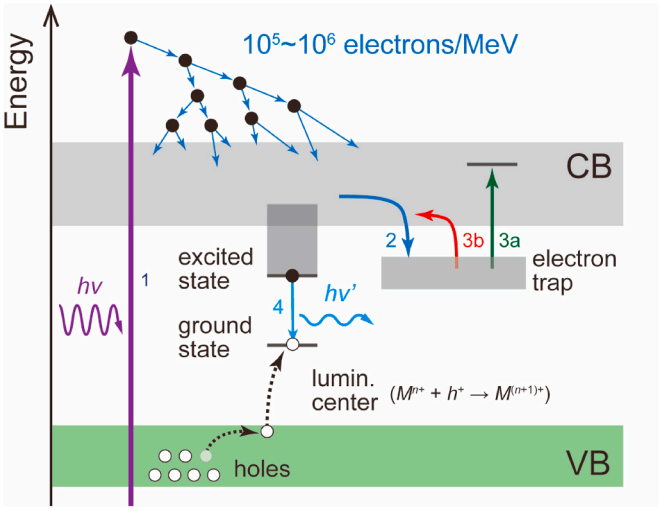

Fig. 1. Schematic illustration of the TL and OSL process, related to the electron trapping and detrapping process: 1. Excitation of electrons with ionizing radiation; 2. Electron trapping; 3a. Optically stimulated electron detrapping; 3b. Thermally stimulated electron detrapping; 4. Radiative electron-hole recombination. During this process, holes generated at the host VB by the ionizing radiation move to the ground state of the luminescence center ion, resulting in the change of the valence state ($M^{n+} + h^+ \rightarrow M^{(n+1)+}$).

hole recombination takes place immediately. However, if energy levels related to impurities or defects are introduced just below the host conduction band (CB), they can act as electron traps, temporarily capturing the excited electrons (arrow 2). The trapped electrons can be released to the CB by optical (arrow 3a) or thermal (arrow 3b) stimulation, and then luminescence is observed upon the carrier recombination (arrow 4). The luminescence related to the optically and thermally stimulating process is called OSL and TL, respectively.

Although they are based on the similar scheme, the OSL technique has some advantages in comparison to the TL technique [17,18]. First, it requires no heating, only optical stimulation. As a result, during the readout processing, OSL is not affected by thermal quenching of the luminescence [17]. Second, by adjusting the stimulating light intensity, fast readouts can be realized, resulting in rapid analysis of a large number of dosimeters (high throughput) [18].

Despite the properties and potential advantages discussed above, the availability of materials with features suitable for some applications is still restricted. For example, the only OSL materials used in commercial dosimetry systems nowadays are Al_2O_3:C and BeO, both of which have relatively slow luminescence lifetimes for laser-scanning 2D dosimetry (35 ms [19] and ~27 μs [20,21], respectively). Al_2O_3:C,Mg has been introduced with a higher concentration of fast luminescence centers (F^+-centers, < 7 ns), but the dominant emission is still from slow luminescence centers (F-centers, 35 ms) [22]. Considering for example a 30.0 cm by 30.0 cm film and ~0.1 mm pixel size, or 9 megapixels, the lifetime has to be lower than ~10 μs for the image to be read within 5 min, assuming that the laser stays three lifetimes over each pixel to avoid pixel bleeding. OSL materials used in image plates (e.g., BaFBr:Eu^{2+}) have typically a high effective atomic number and the OSL signal fades with time after irradiation, which makes them unsuitable for precise dosimetry applications [23–25].

Several new OSL materials have been investigated [26–28]. Magnesium tetraborate, MgB_4O_7, has been attracting attention as a host material for dosimetry based on the OSL or TL technique for several reasons [29–33]. First, it has a low effective atomic number, $Z_{eff} = 8.4$. In radiation dosimetry, materials with an effective atomic number similar to the human body are required to avoid large photon energy dependence; the materials with an effective atomic number similar to water ($Z_{eff} = 7.51$) or tissues ($Z_{eff} = 7.35–7.65$) are suitable. The second reason is the possibility to control the neutron sensitivity by controlling the host content of ^{10}B isotope, which has a high neutron capture cross-section. Ce^{3+}-doped MgB_4O_7 has also been proposed as a potential OSL material for 2D dosimetry, because of the fast luminescence associated with its Ce^{3+} emission due to $5d \rightarrow 4f$ parity allowed transition [34], and also identified by other groups as a potential OSL material for dosimetry [35].

In a previous report, Yukihara et al. evaluated the luminescent properties of Ce^{3+}-doped MgB_4O_7 [33]. Both radioluminescence (RL) and TL were observed in the near-UV region at around 340–360 nm. The fluorescence lifetime of Ce^{3+} $5d \rightarrow 4f$ luminescence in MgB_4O_7, 31.5 ns, was short enough for the use of this material for imaging applications by laser scanning [34], opening the possibility of 2D dosimetry [36]. According to the TL glow curves of MgB_4O_7 doped with a variety of lanthanoid ions, the glow peak of MgB_4O_7:Ce^{3+} was located at around 240 °C, which means that MgB_4O_7:Ce^{3+} has suitable trap depth for OSL dosimetry. In a separate report [37], it was shown that Ce^{3+} and Li^+ co-doped MgB_4O_7 has some attractive dosimetric properties compared to the well-known commercial OSL material Al_2O_3:C. The OSL dose-response of Al_2O_3:C saturates at around 100 Gy, whereas that of MgB_4O_7:Ce^{3+}-Li^+ is proportional to the irradiation dose up to 800 Gy with no saturation, which is desirable for proton and heavy charged particle beams. Besides, it is possible to increase its neutron sensitivity by enriching it with ^{10}B or decrease it by enriching it with ^{11}B. Therefore, the Ce^{3+}-Li^+ co-doped MgB_4O_7 is a promising material for OSL dosimetry. Nevertheless, the MgB_4O_7:Ce^{3+}-Li^+ reported previously [34] suffers from sensitivity changes and anomalous fading of the main dosimetric peak at 240 °C, which motivates the search for new synthesis routes that could improve its dosimetric properties.

To try to improve the dosimetric properties of MgB_4O_7:Ce^{3+}-Li^+, we propose precipitation of the MgB_4O_7 crystals in a borate glass matrix, which is the glass-ceramic (GC) MgB_4O_7. GC materials have many advantages, such as good formability, low cost, mass production, and denser materials than conventional powder packed materials [38,39], which are favorable properties for practical application and commercialization. In this work, the MgB_4O_7 GC samples were prepared by ceramming the as-made magnesium borate glass, and their luminescent properties (photoluminescence (PL), RL, TL, and OSL) of the GC MgB_4O_7:Ce^{3+}-Li^+ were investigated. Besides, the potential of the GC MgB_4O_7:Ce^{3+}-Li^+ for practical OSL application is discussed.

The objective of this work is to demonstrate that MgB_4O_7:Ce^{3+}-Li^+ can be obtained using the glass-ceramic route with intensity and basic properties at least equivalent to those of MgB_4O_7:Ce^{3+}-Li^+ prepared by solution combustion. A complete dosimetric characterization of the samples is beyond the scope of this work, since it requires a more in-depth characterization of the TL and OSL properties than what can be presented here.

2. Experimental details

2.1. Fabrication of samples

Magnesium borate glass samples were prepared with the composition of 25MgO–72B_2O_3–3Li_2O-0.3Ce^{3+} (mol%). To obtain the precipitated MgB_4O_7 crystals in the glass matrix, the molar ratio between B_2O_3 and MgO should be close to 1:2. However, during the melting process at high temperature (~1200 °C), evaporation of B_2O_3 need to be taken into account. The optimized concentration of Li^+ and Ce^{3+} ions was determined in the previous report [37]. Therefore, the composition 25MgO–72B_2O_3–3Li_2O-0.3Ce^{3+} was adopted in this work. The starting chemicals of MgO (99.99%), B_2O_3 (99.9% up), Li_2CO_3 (99.99%), and CeO_2 (99.99%) were weighed and mixed homogeneously in an alumina mortar. The mixture was put into a platinum crucible and calcined at 600 °C for 4 h with the aim of decarbonating Li_2CO_3. After calcination, this mixture was melted at 1200 °C for an hour. The melt was poured on a stainless-steel plate and pressed by another plate. Through this

procedure, the as-made magnesium borate glass sample was fabricated. The glass transition temperature (T_g) and the crystallization temperature (T_x) of the as-made glass sample were evaluated with the differential thermogravimetric analyzer (TG-DTA TG8120, Rigaku, Tokyo, Japan). To obtain the precipitated crystalline phase of MgB_4O_7 in the glass matrix, the as-made glass was heat-treated at 600 °C, 650 °C, 700 °C, 750 °C, 800 °C, and 850 °C for 3 h. Here, some samples were heat-treated over T_x to increase the crystallinity of the MgB_4O_7 phase. The obtained glass-ceramic samples are called GCxx (xx means the ceramming temperature in °C), e.g., GC600 or GC750.

2.2. Characterization

The crystalline phases of all samples were identified with an X-ray diffractometer using Cu Kα radiation (Ultima IV, Rigaku, Tokyo, Japan).

The scanning transmission electron microscope (STEM) images and the elemental mappings with energy dispersive X-ray (EDX) spectroscopy of the microstructure were obtained with a monochromated atomic resolution analytical electron microscope (JEM-ARM200F, JEOL Ltd., Tokyo, Japan).

The photoluminescence excitation (PLE) spectra were measured with a setup consisting of a Xe lamp (CERMAX® PE300BUV, Excelitas Technologies Corp., Waltham, USA), two monochromators (SP-2300i, Princeton Instruments, Acton, USA, and SP-300i, Acton Research Corp., Acton, USA), and a photomultiplier tube (R928, Hamamatsu Photonics, Hamamatsu, Japan). The PLE spectra were calibrated by the spectrum of the Xe lamp (light source) detected by a standard Si photodiode (S1337-1010BQ, Bunkoukeiki & Co., Ltd., Tokyo, Japan). For PL measurements, the samples were excited by dispersed UV light of the Xe lamp ($\lambda = 280$ nm), and the luminescence of the samples were detected with a CCD spectrometer (QE65Pro, Ocean Optics, Largo, USA) connected with an optical fiber. In the case of RL measurements, the samples were excited by Cu Kα characteristic X-ray (40 kV and 30 mA), and the luminescence was detected with the same setup as for PL measurements. The obtained PL and RL spectra were calibrated by the spectrum of a deuterium-tungsten halogen light source (DH-2000, Ocean Optics, Largo, USA).

TL and OSL measurements were carried out using two equipment: a *lexsyg* smart extended reader (Freiberg Instruments GmbH, Freiberg, Germany) and a Risø TL/OSL-DA-20 reader (DTU Nutech, Røskilde, Danmark). The *lexsyg* smart extended reader is equipped with a UV-VIS photomultiplier tube (model 9235QB, Electron Tubes Inc., Rockaway, USA) for luminescence detection, a six-position filter wheel, and a $^{90}Sr/^{90}Y$ source for irradiation (1.53 GBq activity on February 6, 2018, Eckert & Ziegler, Germany, ~50 mGy/s dose rate at the sample position). OSL measurements in the *lexsyg* smart reader were performed using blue light-emitting diodes (centered at 460 nm, 72 mW/cm^2 irradiance). As reported by Gustafson et al. the shorter the stimulation wavelength, the higher the OSL intensity [34]. The optical filters used for detection were Hoya U-340 (5.0 mm total thickness, Hoya corporation, Tokyo, Japan) + Delta BP365/50 EX (Delta Optical Thin Films A/S, Hørsholm, Danmark). The Risø reader is equipped with an Electron Tubes PMD 9107-CP-TTL photomultiplier tube (ET Enterprises, Ltd., Uxbridge, UK) for light detection, an Automated Detection and Stimulation Head (DASH) and a beta irradiation unit (1.48 GBq, Sr-90 source, Eckert & Ziegler Nuclitec GmbH, Brunschweig, Germany). The OSL measurements in the Risø reader were performed with blue LEDs (centered at 470 nm, 80 mW/cm^2 irradiance). The optical filters used for detection were Hoya U-340 filters (7.5 mm total thickness, Hoya corporation, Tokyo, Japan). TL measurements were performed at 5 °C/s in the presence of N_2 in both instruments. Samples measured in ceramic form had ~20.2–45.2 mg. Samples measured in powder form had typically ~2.0–4.0 mg. When relevant, the signal was normalized by the sample mass for comparison.

3. Results and discussions

3.1. Thermal behavior of as-made glass

Fig. 2 shows the differential thermal analysis (DTA) curve of the as-made magnesium borate glass sample. From the position of a sharp exothermic peak, T_x was 716 °C. The baseline below and over ~625 °C was different, which means the glass transition took place at around 625 °C. According to the analysis of this DTA curve, T_g of the as-made glass sample was estimated to be 624 °C. One endothermic peak was observed at around 820 °C, which is related to the partial melting of the glass phase. Because of this melting, the GC samples cerammed over 900 °C could not be prepared in a proper shape.

3.2. Structural analysis

Fig. 3 shows the X-ray diffraction (XRD) patterns of the as-made glass and all the prepared GC samples with the reference pattern for orthorhombic MgB_4O_7 (PDF #01-076-0666), which belongs to the space group *Pbca* (No. 61). The as-made glass sample shows two halo peaks due to the amorphous phase of the magnesium borate glass. For the GC samples, the MgB_4O_7 crystals were precipitated after heat treatment at and above 600 °C. Only in the XRD pattern of GC600, the weak halo peaks of the amorphous phase were still observed. Therefore, the ceramization process of MgB_4O_7 was almost completed by heat treatment above 650 °C. Although almost all diffraction peaks were assigned to orthorhombic MgB_4O_7, one weak peak of an impurity phase, assigned to triclinic $Mg_2B_2O_5$ (PDF #01-083-0625), was observed at $2\theta = \sim 35°$. With increasing heat treatment temperature, the peak intensity of impurity $Mg_2B_2O_5$ increases. To prevent this B_2O_3-poor phase from being precipitated, heat treatment at lower temperatures (650–750 °C) is a suitable condition for the preparation of the GC MgB_4O_7 samples.

In the unit cell of orthorhombic MgB_4O_7, there are eight interstitial sites coordinated by some BO_3 and BO_4 units. From this point of view, Ce^{3+} ions, which are the luminescence center and have the larger ionic radius ($r = 1.01$ Å, CN = 6) than Mg^{2+} ions ($r = 0.72$ Å, CN = 6) [40], can prefer these large interstitial sites to the Mg^{2+} sites. At the same time, Li^+ ions ($r = 0.76$ Å, CN = 6) [40] are able to occupy the Mg^{2+} site, which results in the charge compensation for the trivalent Ce^{3+} ions. With the Kröger-Vink notation, the Li^+ ions at this site can be denoted as $Li_{Mg}^{'}$.

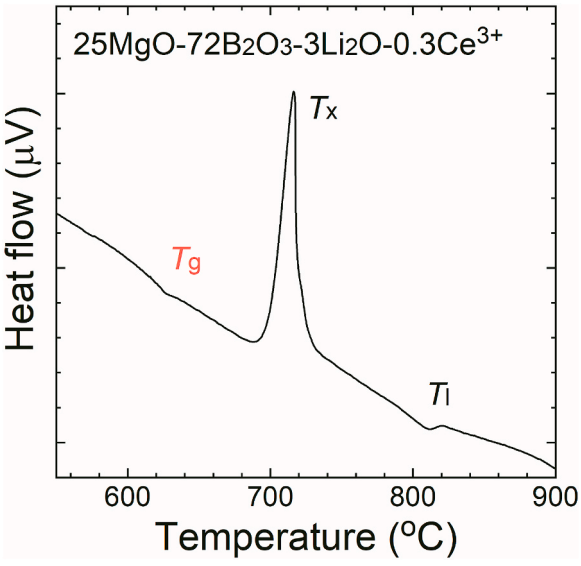

Fig. 2. DTA curve of the as-made glass sample. T_g, T_x, and T_l mean the glass transition, crystallization, and partial melting temperature, respectively.

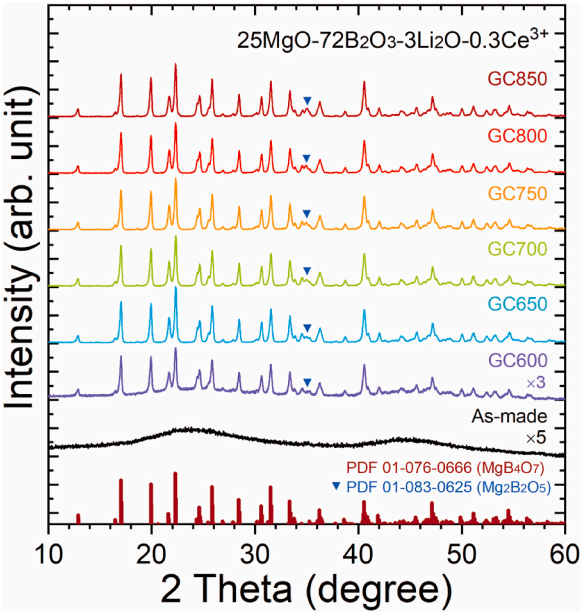

Fig. 3. XRD patterns of the prepared samples with the reference data of crystalline MgB_4O_7 (PDF #01-076-0666).

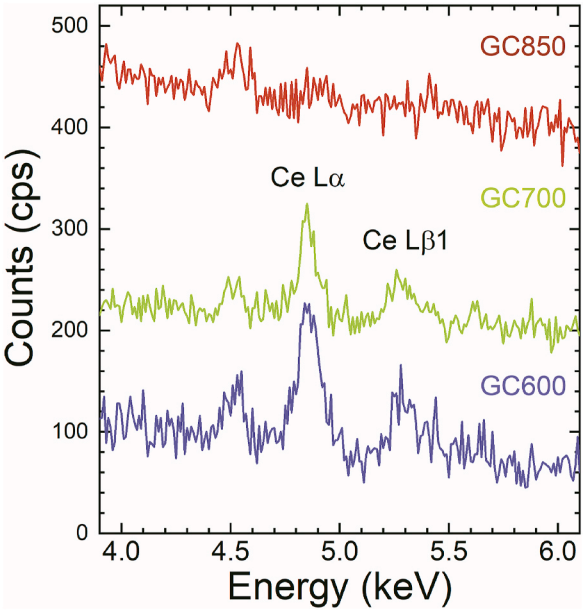

Fig. 5. EDX spectra of GC600, GC700, and GC850.

Fig. 4 shows the STEM images and elemental mappings with EDX for different elements (Mg, B, O, and Ce) for GC700. Before the STEM measurements, the GC samples were crushed into powder and then put on a microgrid. When the images are taken in low-magnification, the observed particles are not the precipitated MgB_4O_7 crystals but the pulverized GCs. Some rod-shaped particles in the order of hundreds of nm were observed at around the edge of the pulverized GCs. While B and O were spread out homogeneously and characteristic X-ray intensity of B and O was proportional to the thickness of the sample, Mg was concentrated on these particles, resulting in the high contrast mapping. By taking into account this localization of Mg and the XRD patterns in Fig. 3, these particles were microcrystals of orthorhombic MgB_4O_7, and the glass matrix had boron-rich composition compared with the composition of MgB_4O_7. Ce^{3+} ions were also located homogeneously in both the crystalline and glass phases. Fig. 5 shows the EDX spectra of GC600, GC700, and GC850. For GC600 and GC700, two peaks assigned to Ce Lα and Ce Lβ were observed at around 4.85 and 5.28 keV, respectively. These signals were feeble because of the low Ce^{3+} concentration. However, there was no signal attributed to Ce in GC850, because the microcrystals of Ce^{3+}-doped MgB_4O_7 aggregated due to the high-temperature heat treatment and no longer existed on the surface of particles.

Ce^{3+} and Li^+ concentrations were determined by following the previous report [37] to obtain the sample with the best dosimetric performance of the GC MgB_4O_7:Ce^{3+}-Li^+. Due to the co-existence of the glass and crystalline phase, the actual Ce^{3+} and Li^+ concentrations in the MgB_4O_7 crystals can differ from the assumed one. Considering the very small volume fraction of the glassy phase, the deviation of the concentration should be small. Moreover, the Ce^{3+} concentration is also affected by the oxidation state. The Ce^{4+} state is stable in the glass phase of very high basicity through the melt-quenching method in the strong oxidizing atmosphere. Since the magnesium borate glass has low basicity, only a very small amount of Ce can be oxidized into the tetravalence state. A significant amount of Ce^{4+} ions would interact with Ce^{3+} ions through the intervalence charge transfer, resulting in the brownish color of the sample. The color of the GC samples is white, and no strong absorption is observed in the visible range (the diffuse reflectance spectra are shown in Fig. S6), indicating the absence of Ce^{4+}.

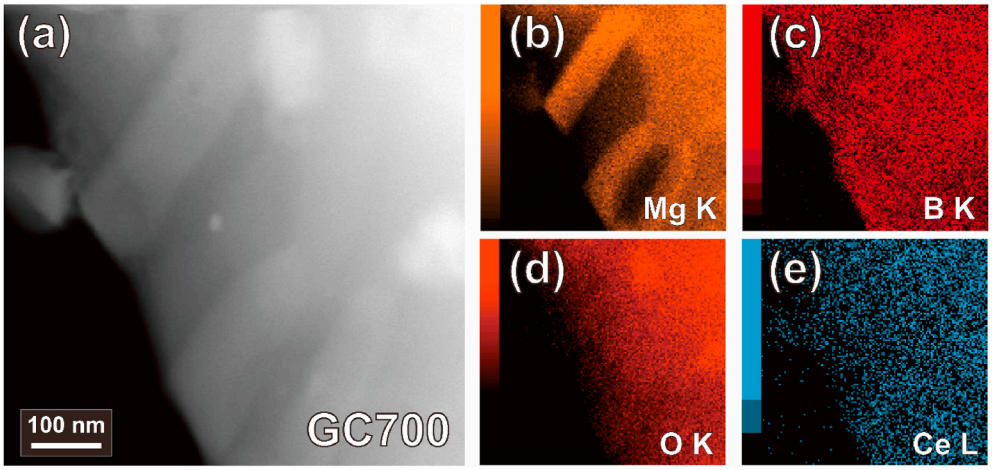

Fig. 4. (a) STEM image of GC700, and (b)~(e) EDX mappings for different elements (Mg, B, O, and Ce).

3.3. PL properties of magnesium borate glass and glass-ceramic samples

Based on spectroscopy, the luminescent properties of the prepared samples were investigated. Fig. 6(a) shows the PLE spectra monitoring at 380 nm. The as-made glass sample showed the weak excitation bands peaking at 315 nm. These bands are assigned to the $5d \leftarrow 4f$ transition of Ce^{3+} ions in the glass phase. For the GC samples (GC650~850), the broad excitation bands were observed in the UV region below 350 nm, having three major components peaking at 320, 290, and 270 nm, respectively. In the previous research reported by Gustafson et al. [34], the ceramic MgB_4O_7:Ce^{3+} sample showed the typical Ce^{3+} $5d \leftarrow 4f$ excitation bands peaking at ~320 nm, ~293 nm, and ~270 nm. Therefore, these excitation bands are assigned to the $5d \leftarrow 4f$ transition of Ce^{3+} ions in the crystalline phase of MgB_4O_7. Despite precipitation of the crystalline MgB_4O_7, the GC600 showed a similar spectral shape to the as-made glass. Judging from the weak XRD peak intensity described in Fig. 3, this similarity is because Ce^{3+} luminescence in the glass phase was dominant due to the low crystallinity of MgB_4O_7. For the GC850 sample, the PLE intensity was much weaker than other samples. The cause of this phenomenon will be discussed in the following paragraph.

Fig. 6(b) shows the PL spectra under UV excitation ($\lambda_{ex} = 280$ nm). The samples showed UV-to-blue luminescence ranging under 300–500 nm, which is assigned to the $5d \rightarrow 4f$ transition of Ce^{3+} ions. For the as-made glass and GC600 samples, where most of the Ce^{3+} ions are accommodated in the glass matrix, the broad emission bands were located at the UV region, peaking at ~330 nm ($= 3.03 \times 10^4$ cm^{-1}). On the other hand, for other GC samples, the PL bands attributed to the Ce^{3+} $5d \rightarrow 4f$ transition in the MgB_4O_7 host are peaked at ~370 nm ($= 2.70 \times 10^4$ cm^{-1}), and the spectral shape of these bands was similar to the previous report [34]. When Ce^{3+} ions are in the coordinated environment, $5d$ excited levels get depressed by the nephelauxetic effect by surrounding anions and split by the crystal field [41,42]. In both the glass and crystalline phases, Ce^{3+} ions are surrounded by the same anion species, oxide anions of borate groups. Accordingly, the degree of the centroid shift for the as-made glass and GC samples should be similar, and the energy difference of luminescence between them ($= 3.3 \times 10^3$ cm^{-1}) can mainly be due to the ligand field effect. In other words, Ce^{3+} ions in the crystalline MgB_4O_7 phase show red-shifted luminescence because of the crystal field splitting derived from the ordered interstitial sites. The Ce^{3+} luminescence intensity in glass phase was weaker than that in the MgB_4O_7 crystalline phase. This is because the high concentration of intrinsic disordered defects in amorphous phase, which can cause luminescence quenching through nonradiative relaxation paths. For GC850, the PL intensity was also quite weak, and the peak wavelength was blue-shifted, compared with other GC samples. As this spectral shape was similar to the PL bands in the glass matrix discussed above, Ce^{3+} luminescence in the glass phase, which was slightly present between the MgB_4O_7 particles, was mainly observed. In the MgB_4O_7 crystalline phase in GC850, the concentration quenching of Ce^{3+} $5d \rightarrow 4f$ luminescence occurred, because the distance between adjacent Ce^{3+} ions got shorter owing to the aggregation of MgB_4O_7:Ce^{3+} crystals.

3.4. RL properties of magnesium borate glass and glass-ceramic samples

In Fig. 6(c), the RL spectra excited by Cu Kα characteristic X-ray at room temperature are shown. The as-made glass sample showed very weak emission under X-ray irradiation; it can be difficult to excite $4f$ electrons of Ce^{3+} ions in the glass matrix with ionizing radiation. In contrast, the GC samples showed stronger RL intensity than the as-made glass sample; that is, X-ray could excite the Ce^{3+} ions efficiently in the crystalline phase. This is the reason the GC600 and GC850, in which the Ce^{3+} luminescence in the glass phase was dominant (see Section 3.3), showed weak RL.

As with the PL spectra, the characteristic Ce^{3+} $5d \rightarrow 4f$ emission bands were observed, peaking at ~340 and ~360 nm. However, compared with the PL spectra shown in Fig. 6(b), the two emission peaks in the RL spectra were clearly observed, and the width of the bands was narrower. The possible explanation for these narrow bands is that luminescence via electron-hole recombination takes place only on interstitial Ce^{3+} ions, not on Ce^{3+} in the disordering environment, due to the efficient energy transfer from the host material. In the energetic scale, the energy difference between these two peaks is ~2000 cm^{-1}, which is a similar value to the energy difference between $^2F_{5/2}$ and $^2F_{7/2}$ levels for Ce^{3+} due to the spin-orbital interaction of the $4f$ ground state. These two bands can be assigned to the transitions from the lowest excited level $5d_1$ to the $^2F_{5/2}$ and $^2F_{7/2}$ levels.

Despite excitation with the high-power ionizing radiation (~8.0 keV, 1200 W), the RL intensity was similar in the order of magnitude as the PL intensity, which means that the efficiency of RL was not so high. As previously stated in the introduction, the excitation with ionizing radiation creates a lot of electron-hole pairs, which will only produce Ce^{3+} emission if the excitons become localized on the Ce^{3+}, or if Ce^{3+} captures a hole followed by an electron with the valence state change ($Ce^{3+} + h^+ \rightarrow Ce^{4+}$). Nevertheless, since there are other recombination routes, the RL intensity is normally much less efficient than direct excitation of the Ce^{3+} ions.

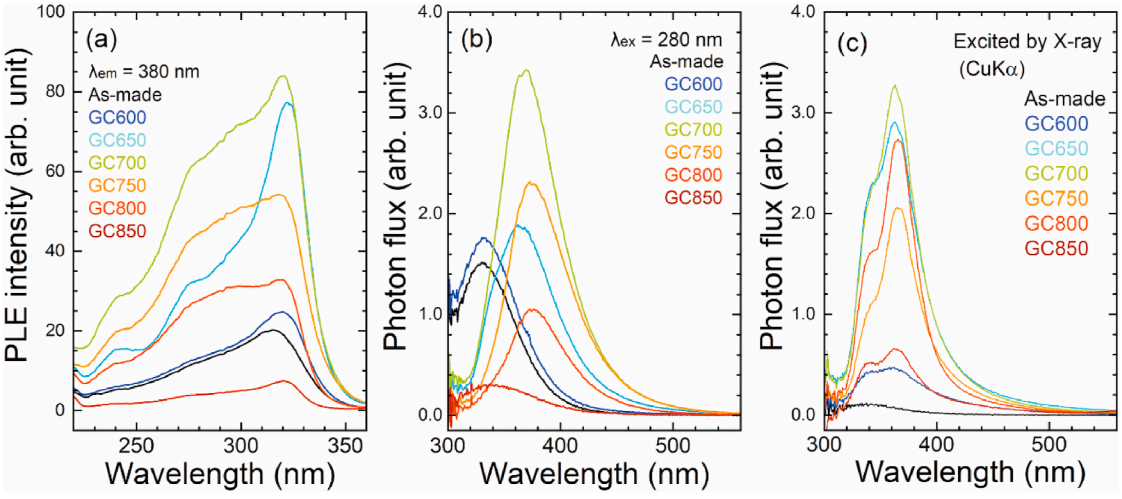

Fig. 6. (a) PLE spectra of all the samples, monitoring Ce^{3+} emission at 380 nm. (b) PL spectra of all the samples under UV ($\lambda_{ex} = 280$ nm) illumination. (c) RL spectra of all the samples under Cu Kα characteristic X-ray illumination.

3.5. TL properties of the glass-ceramic samples

Fig. 7(a) shows the TL glow curves of the GC samples after $^{90}Sr/^{90}Y$ β-ray irradiation. During the synthesis process, the GC samples were heat-treated over the maximum temperature of TL measurements (400 °C) for 3 h. The as-made and GC samples did not show any endo- and exothermic peak in the DTA curves below 500 °C (shown in Fig. S2), indicating that the nucleation and crystal growth process did not take place during TL measurements.

Whereas only GC600, which still has a large amount of glass matrix, showed weak TL, all GC samples show two TL glow peaks at ~100 and ~220 °C (labeled peak 1 and peak 2, respectively), whose intensity variations show similar trends to those of PL and RL intensities. These two glow peak temperatures are related to their electron trap depth, which is the activation energy from some trap levels (donor level) to the host CB; peak 1 and peak 2 are related to shallow and deep electron traps, respectively. According to the previous work [29,33,43–51], it is well-known that lanthanoid and lithium ions in the crystal lattice of MgB_4O_7 can help form electron trapping centers related to impurity-related defects. Notably, the shape of the TL glow peak 2 for GC samples was similar to that of the powder MgB_4O_7:Ce^{3+}-Li^+ prepared through the combustion synthesis method, except for GC600 [34]. For GC600, the TL intensity of peak 2 was quite weak because the ceramization process was not completed. Therefore, these TL glow curves indicate that the precipitation of MgB_4O_7:Ce^{3+}-Li^+ worked well for the electron trap formation. With increasing heat treatment temperature, peak 2 was shifted toward the high-temperature side, and GC850 showed an additional TL glow peak at ~300 °C. Considering the impurity phase confirmed by XRD, it suggests that this additional peak at the higher temperature region can be assigned to the electron traps related to the impurity $Mg_2B_2O_5$ phase.

For further investigation into the behavior of electron traps, the TL glow curves of GC750 with different delays between $^{90}Sr/^{90}Y$ β-ray irradiation and TL readout (0–60 min) are shown in Fig. 7(b). Those of the other samples are shown in the supplementary materials, Fig. S7. The TL intensity of peak 1 declined gradually with the delay. This decline is called fading, which is interpreted as electron release from the trap levels via the thermally activating process at room temperature [52,53]. This fading is undesirable in dosimetry, because a time-dependent TL signal makes the precise estimation of the radiation dose more difficult. In contrast, the TL intensity of peak 2 associated with the deep trap was almost unchanged, which indicates that the electrons in the associated trapping centers are stable.

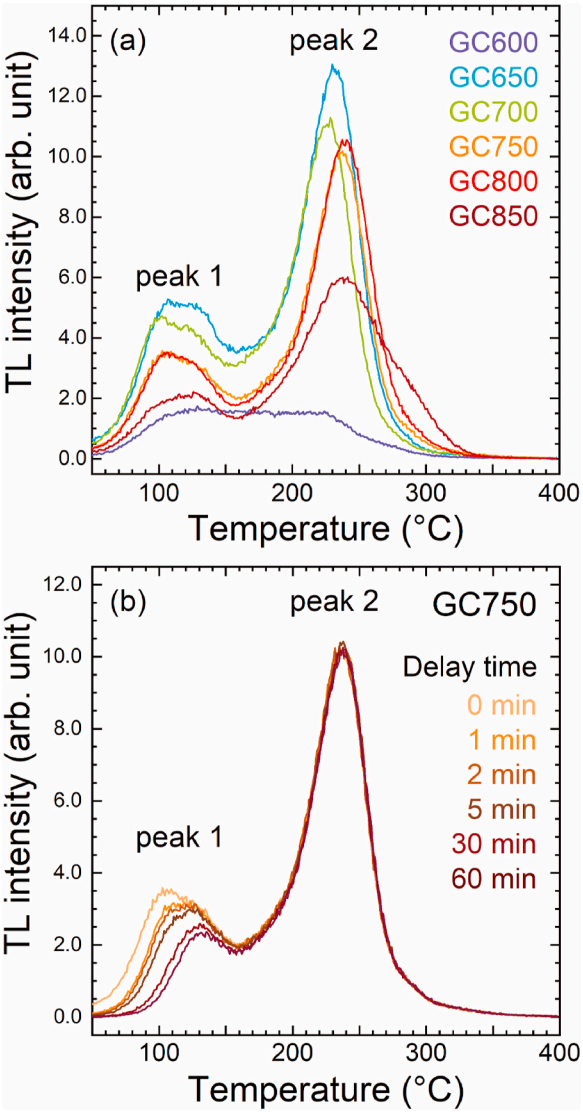

Fig. 7. TL glow curves of (a) all the GC samples, and (b) GC700 with different delay time (0–60 min).

3.6. OSL properties of the glass-ceramic samples

The GC samples show OSL under visible light stimulation due to the electron traps confirmed by the TL glow curves. The typical OSL emission and stimulation spectra of the GC700 are shown in the supplementary materials, Fig. S8 and S9. For a test and comparison of the performance of each GC sample as an OSL dosimeter, the OSL signal was measured with various delays (1–600 min) after β-ray irradiation.

Fig. 8 shows the total OSL fading curves of each sample, where the OSL signal was plotted as a function of delay between irradiation and readout. All GC samples show a monotonic decline of the OSL intensity due to fading. As expected from the RL spectra (Fig. 6(c)) and the TL glow curves (Fig. 7(a)), the total OSL intensity of GC650 and GC700 were high. However, they were still declining between 300 and 600 min, indicating that further fading may take place. On the other hand, for GC750 and GC800, the total OSL intensity stays essentially unchanged after 300 min delay, which indicates possibly low fading of the OSL intensity above 600 min, allowing a more precise estimation of the radiation dose.

To examine the stability of the electrons captured by traps, the fading ratio, defined as the ratio of the OSL signal with 600 min delay to the

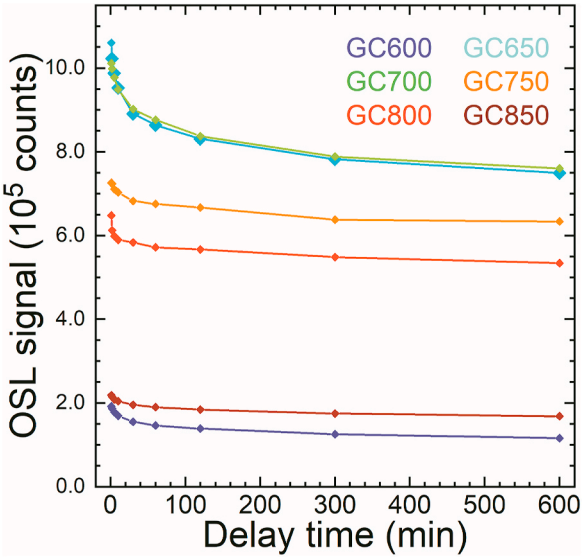

Fig. 8. Fading curves of total OSL signal for all the GC samples.

initial OSL signal, can be a good indicator. The fading ratio of each sample is listed in Table 1. Although GC650 and GC 700 showed very strong OSL, their fading ratio is high, which implies that around one-fourth of trapped electrons is lost after 600 min delay; they are less suitable for dosimetry applications. By contrast, GC750 and GC800 show low fading ratios, 12.7%, and 17.5%, respectively, due to the deep traps which show little fading. These characteristics are very suitable for the OSL dosimetry of high performance.

Finally, the OSL intensity of the GC700 sample was compared with two OSL materials, the MgB_4O_7:Ce^{3+}-Li^+ sample prepared by solution combustion (SC) described by Gustafson et al. [34] and commercial Al_2O_3:C. To improve the comparison, all samples were used in powder form and the results were normalized by the powder mass. The GC700 sample was crushed using an agate mortar and pestle. Approximate 2.0 mg MgB_4O_7:Ce^{3+}-Li^+ SC, 4.1 mg of GC700 sample, and 6.4 mg of Al_2O_3:C were used in each cup. Nevertheless, one must keep in mind that this is only an order of magnitude comparison, because other factors such as grain size and the different optimum stimulation/detection wavelength for MgB_4O_7:Ce^{3+}-Li^+ and Al_2O_3:C were not taken into account at this stage. The Hoya U-340 filters used in the Risø readers are not optimum for Al_2O_3:C, because they block a large part of the main F-center emission band of this material.

The OSL curves of the samples are shown in Fig. 9. Here, the y axis is a logarithmic scale for better visualization of the OSL curve. The results demonstrate that the OSL intensity of GC700 is comparable to that of commercial Al_2O_3:C and to that of MgB_4O_7:Ce^{3+}-Li^+ powder reported in previous studies [34]. The advantage of the GC samples in comparison with the MgB_4O_7:Ce^{3+}-Li^+ SC sample is the potential lower fading of the signal because of the higher crystallinity of MgB_4O_7 in the ceramic, since the TL curves show that the main dosimetric peak at ~220 °C is reproducible and does not fade within the experimental conditions used here.

This work demonstrates that MgB_4O_7:Ce^{3+}-Li^+ as bright as the one obtained by solution combustion can also be obtained by the glass-ceramic route, but a more detailed dosimetric comparison between the different materials is planned.

4. Conclusions

To expand the possibility of the prospective dosimetric material, Ce^{3+} and Li^+ co-doped MgB_4O_7, the GC samples of MgB_4O_7:Ce^{3+}-Li^+ were successfully synthesized by ceramming a magnesium borate glass with the composition of 25MgO–72B_2O_3–3Li_2O-0.3Ce^{3+} at 600 °C, 650 °C, 700 °C, 750 °C, 800 °C, and 850 °C. It was confirmed by XRD that the obtained GC samples had the MgB_4O_7 crystals as the main phase with a small amount of impurity $Mg_2B_2O_5$ phase. The GC samples showed a typical blue PL band due to the Ce^{3+} $5d \rightarrow 4f$ transition under UV illumination, whose peak was red-shifted from the peak in the as-made glass. For the GC samples, the RL bands of Ce^{3+} luminescence under X-ray irradiation were narrower than the PL bands because the Ce^{3+} ions in the MgB_4O_7 phase can selectively be excited. In the TL glow curves after β-ray irradiation, the GC samples showed two TL glow peaks at ~100 °C and ~220 °C. Due to the presence of the shallow electron traps, the fading of TL and OSL took place. Considering the fading ratio of the OSL intensity stimulated by a blue LED, GC750 and GC800 show good stability for the radiation dose storage. These results show that GC750 and GC800 have the potential to be an excellent material for dosimetry if the influence of shallow traps can be reduced either during the synthesis process or by application of a pre-heating before the OSL readout.

CRediT author statement

Yuuki Kitagawa: Conceptualization, Methodology, Formal analysis, Investigation, Writing – original draft, Visualization Eduardo G. Yukihara: Conceptualization, Methodology, Formal analysis, Writing – review & editing, Supervision, Project administration, Funding acquisition Setsuhisa Tanabe: Conceptualization, Methodology, Writing – review & editing, Supervision, Project administration, Funding acquisition.

Table 1
Fading ratio of OSL signal for all the GC samples. Charged GC samples were stimulated by the blue LED after each delay time (0–600 min).

Sample	GC600	GC650	GC700	GC750	GC800	GC850
Fading ratio (%)	39.8	29.3	24.8	12.7	17.5	22.9

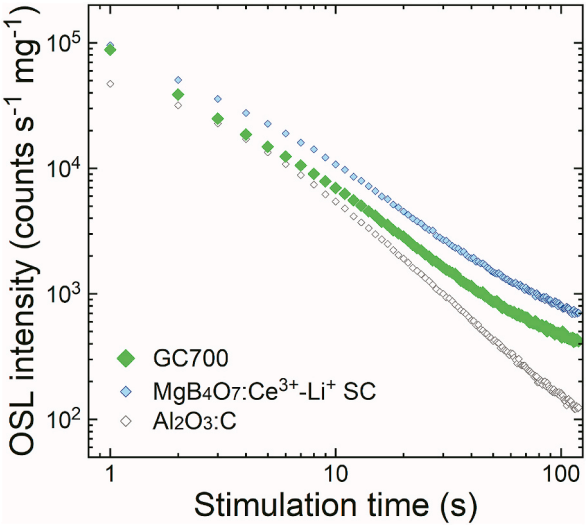

Fig. 9. Comparison between the OSL intensity of MgB_4O_7:Ce^{3+}-Li^+ sample (~2.0 mg) prepared by combustion synthesis, MgB_4O_7:Ce^{3+}-Li^+ GC700 sample (4.1 mg), and commercial Al_2O_3:C (6.4 mg). All samples were measured in powder form and the OSL intensity was normalized by the sample mass.

Declaration of competing interest

The authors declare that they have no known competing financial interests or personal relationships that could have appeared to influence the work reported in this paper.

Acknowledgements

This work was supported by Kyoto University Microstructural Characterization Platform as a program of "Nanotechnology Platform" of the Ministry of Education, Culture, Sports, Science, and Technology (MEXT), Japan, and KAKENHI for the Grant-in-Aid for Scientific Research B (Grant Numbers JP19H02798 and JP16H06441) and JSPS Fellow (Grant Number JP19J23280) from JSPS. The Risø TL/OSL-DA-20 reader (DTU Nutech, Denmark) was acquired with partial support from the Swiss National Science Foundation (R'Equip project 206021_177028).

Appendix A. Supplementary data

Supplementary data to this article can be found online at https://doi.org/10.1016/j.jlumin.2020.117847.

References

[1] I.J. Das, G.X. Ding, A. Ahnesjö, Small fields: nonequilibrium radiation dosimetry, Med. Phys. 35 (2008) 206–215, https://doi.org/10.1118/1.2815356.
[2] F. Borne, D. Delacroix, J.M. Gelé, D. Massé, F. Amiranoff, Radiation protection for an ultra-high intensity laser, Radiat. Protect. Dosim. 102 (2002) 61–70, https://doi.org/10.1093/oxfordjournals.rpd.a006074.

[3] R.J. Clarke, D. Neely, R.D. Edwards, P.N.M. Wright, K.W.D. Ledingham, R. Heathcote, P. McKenna, C.N. Danson, P.A. Brummitt, J.L. Collier, P.E. Hatton, S. J. Hawkes, C. Hernandez-Gomez, P. Holligan, M.H.R. Hutchinson, A.K. Kidd, W. J. Lester, D.R. Neville, P.A. Norreys, D.A. Pepler, T.B. Winstone, R.W.W. Wyatt, B. E. Wyborn, Radiological characterisation of photon radiation from ultra-high-intensity laser–plasma and nuclear interactions, J. Radiol. Prot. 26 (2006) 277–286, https://doi.org/10.1088/0952-4746/26/3/002.
[4] D.J. O'Brien, N. Schupp, S. Pencea, J. Dolan, G.O. Sawakuchi, Dosimetry in the presence of strong magnetic fields, J. Phys. Conf. Ser. 847 (2017), 012055, https://doi.org/10.1088/1742-6596/847/1/012055.
[5] G.F. Knoll, Radiation Detection and Measurement, third ed., John Wiley and Sons Inc., New York, 2000.
[6] T. Yamamoto, D. Maki, F. Sato, Y. Miyamoto, H. Nanto, T. Iida, The recent investigations of radiophotoluminescence and its application, Radiat. Meas. 46 (2011) 1554–1559, https://doi.org/10.1016/j.radmeas.2011.04.038.
[7] Y. Miyamoto, Y. Takei, H. Nanto, T. Kurobori, A. Konnai, T. Yanagida, A. Yoshikawa, Y. Shimotsuma, M. Sakakura, K. Miura, K. Hirao, Y. Nagashima, T. Yamamoto, Radiophotoluminescence from silver-doped phosphate glass, Radiat. Meas. 46 (2011) 1480–1483, https://doi.org/10.1016/j.radmeas.2011.05.048.
[8] Y.S. Horowitz, Thermoluminescence and Thermoluminescent Dosimetry, CRC Press, Boca Raton, 1983.
[9] L. Bøtter-Jensen, S.W.S. McKeever, A.G. Wintle, Optically Stimulated Luminescence Dosimetry, Elsevier B.V., Amsterdam, 2003, https://doi.org/10.1016/B978-0-444-50684-9.X5077-6.
[10] S. McKeever, E.G. Yukihara, Optically Stimulated Luminescence : Fundamentals and Applications, John Wiley & Sons, Ltd, Chichester, 2011.
[11] M.F. Ahmed, N. Shrestha, S. Ahmad, E. Schnell, M.S. Akselrod, E.G. Yukihara, Demonstration of 2D dosimetry using Al_2O_3 optically stimulated luminescence films for therapeutic megavoltage x-ray and ion beams, Radiat. Meas. 106 (2017) 315–320, https://doi.org/10.1016/j.radmeas.2017.04.010.
[12] K. Idri, L. Santoro, E. Charpiot, J. Herault, A. Costa, N. Aillères, R. Delard, J. R. Vaillé, J. Fesquet, L. Dusseau, Quality control of intensity modulated radiation therapy with optically stimulated luminescent films, IEEE Trans. Nucl. Sci. 51 (2004) 3638–3641, https://doi.org/10.1109/TNS.2004.839299.
[13] L.F. Nascimento, W. Crijns, G. Goveia, Z. Mirotta, L.F. Souza, F. Vanhavere, C. Saldarriaga Vargas, M. De Saint-Hubert, 2D reader for dose mapping in radiotherapy using radiophotoluminescent films, Radiat. Meas. 129 (2019) 106202, https://doi.org/10.1016/j.radmeas.2019.106202.
[14] P.A. Rodnyi, Physical Processes in Inorganic Scintillators, CRC Press, Boca Raton, 1997.
[15] Y. Horowitz, L. Oster, I. Eliyahu, Review of dose-rate effects in the thermoluminescence of LiF:Mg,Ti (harshaw), Radiat. Protect. Dosim. 179 (2018) 184–188, https://doi.org/10.1093/rpd/ncx248.
[16] C.K. Spindeldreier, O. Schrenk, M.F. Ahmed, N. Shrestha, C.P. Karger, S. Greilich, A. Pfaffenberger, E.G. Yukihara, Feasibility of dosimetry with optically stimulated luminescence detectors in magnetic fields, Radiat. Meas. 106 (2017) 346–351, https://doi.org/10.1016/j.radmeas.2017.03.018.
[17] S.W.S. McKeever, Optically stimulated luminescence dosimetry, Nucl. Instrum. Methods Phys. Res. B. 184 (2001) 29–54, https://doi.org/10.1016/S0168-583X(01)00588-2.
[18] S.W.S. McKeever, New millennium frontiers of luminescence dosimetry, Radiat. Protect. Dosim. 100 (2002) 27–32, https://doi.org/10.1093/oxfordjournals.rpd.a005865.
[19] M.S. Akselrod, N. Agersnap Larsen, V. Whitley, S.W.S. McKeever, Thermal quenching of F-center luminescence in Al_2O_3:C,, J. Appl. Phys. 84 (1998) 3364–3373, https://doi.org/10.1063/1.368450.
[20] E.G. Yukihara, Luminescence properties of BeO optically stimulated luminescence (OSL) detectors, Radiat. Meas. 46 (2011) 580–587, https://doi.org/10.1016/j.radmeas.2011.04.013.
[21] E. Bulur, B.E. Saraç, Time-resolved OSL studies on BeO ceramics, Radiat. Meas. 59 (2013) 129–138, https://doi.org/10.1016/j.radmeas.2013.04.009.
[22] G. Denis, M.G. Rodriguez, M.S. Akselrod, T.H. Underwood, E.G. Yukihara, Time-resolved measurements of optically stimulated luminescence of Al_2O_3:C and Al_2O_3:C,Mg, Radiat. Meas. 46 (2011) 1457–1461, https://doi.org/10.1016/j.radmeas.2011.06.054.
[23] C. Wouter, V. Dirk, L. Paul, D. Tom, A reusable OSL-film for 2D radiotherapy dosimetry, Phys. Med. Biol. 62 (2017) 8441–8454, https://doi.org/10.1088/1361-6560/aa8de6.
[24] H.H. Li, A.L. Gonzalez, H. Ji, D.M. Duggan, Dose response of BaFBrI:Eu^{2+} storage phosphor plates exposed to megavoltage photon beams, Med. Phys. 34 (2006) 103–111, https://doi.org/10.1118/1.2400617.
[25] E. Ariga, S. Ito, S. Deji, T. Saze, K. Nishizawa, Development of dosimetry using detectors of diagnostic digital radiography systems, Med. Phys. 34 (2006) 166–174, https://doi.org/10.1118/1.2402911.
[26] E.G. Yukihara, S.W.S. McKeever, Optically stimulated luminescence (OSL) dosimetry in medicine, Phys. Med. Biol. 53 (2008) R351–R379, https://doi.org/10.1088/0031-9155/53/20/R01.
[27] A.S. Pradhan, J.I. Lee, J. Kim, Recent developments of optically stimulated luminescence materials and techniques for radiation dosimetry and clinical applications, J. Med. Phys. 33 (2008) 85–99, https://doi.org/10.4103/0971-6203.42748.
[28] B.A. Doull, L.C. Oliveira, D.Y. Wang, E.D. Milliken, E.G. Yukihara, Thermoluminescent properties of lithium borate, magnesium borate and calcium sulfate developed for temperature sensing, J. Lumin. 146 (2014) 408–417, https://doi.org/10.1016/j.jlumin.2013.10.022.
[29] M. Prokić, Development of highly sensitive $CaSO_4$:Dy/Tm and MgB_4O_7:Dy/Tm sintered thermoluminescent dosimeters, Nucl. Instrum. Methods 175 (1980) 83–86, https://doi.org/10.1016/0029-554X(80)90262-1.
[30] C.M.H. Driscoll, S.J. Mundy, J.M. Elliot, Sensitivity and fading characteristics of thermoluminescent borate, Radiat. Protect. Dosim. 1 (1981) 135–137, https://doi.org/10.1093/oxfordjournals.rpd.a079967.
[31] M. Prokić, L. Bøtter-Jensen, Comparison of main thermoluminescent properties of some TL dosemeters, Radiat. Protect. Dosim. 47 (1993) 195–199, https://doi.org/10.1093/oxfordjournals.rpd.a081731.
[32] M. Prokić, Individual monitoring based on magnesium borate, Radiat. Protect. Dosim. 125 (2006) 247–250, https://doi.org/10.1093/rpd/ncl116.
[33] E.G. Yukihara, E.D. Milliken, B.A. Doull, Thermally stimulated and recombination processes in MgB_4O_7 investigated by systematic lanthanide doping, J. Lumin. 154 (2014) 251–259, https://doi.org/10.1016/j.jlumin.2014.04.038.
[34] T.D. Gustafson, E.D. Milliken, L.G. Jacobsohn, E.G. Yukihara, Progress and challenges towards the development of a new optically stimulated luminescence (OSL) material based on MgB_4O_7:Ce,Li, J. Lumin. 212 (2019) 242–249, https://doi.org/10.1016/j.jlumin.2019.04.028.
[35] L.F. Souza, A.M.B. Silva, P.L. Antonio, L.V.E. Caldas, S.O. Souza, F. d'Errico, D. N. Souza, Dosimetric properties of MgB_4O_7:Dy,Li and MgB_4O_7:Ce,Li for optically stimulated luminescence applications, Radiat. Meas. 106 (2017) 196–199, https://doi.org/10.1016/j.radmeas.2017.02.009.
[36] N. Shrestha, D. Vandenbroucke, P. Leblans, E.G. Yukihara, Feasibility studies on the use of MgB_4O_7:Ce,Li-based films in 2D optically stimulated luminescence dosimetry, Phys. Open (2020), https://doi.org/10.1016/j.physo.2020.100037.
[37] E.G. Yukihara, B.A. Doull, T. Gustafson, L.C. Oliveira, K. Kurt, E.D. Milliken, Optically stimulated luminescence of MgB_4O_7:Ce,Li for gamma and neutron dosimetry, J. Lumin. 183 (2017) 525–532, https://doi.org/10.1016/j.jlumin.2016.12.001.
[38] S. Tanabe, S. Fujita, A. Sakamoto, S. Yamamoto, Glass ceramics for solid state lighting, Ceram. Trans. 173 (2006) 19–25, https://doi.org/10.1002/9781118407974.ch3.
[39] T. Nakanishi, S. Tanabe, Novel Eu^{2+}-activated glass ceramics precipitated with green and red phosphors for high-power, IEEE J. Sel. Top. Quant. Electron. 15 (2009) 1171–1176, https://doi.org/10.1109/JSTQE.2009.2014396.
[40] R.D. Shannon, Revised effective ionic radii and systematic studies of interatomic distances in halides and chalcogenides, Acta Crystallogr. A 32 (1976) 751–767, https://doi.org/10.1107/S0567739476001551.
[41] Z. Xia, A. Meijerink, Ce^{3+}-Doped garnet phosphors: composition modification, luminescence properties and applications, Chem. Soc. Rev. 46 (2017) 275–299, https://doi.org/10.1039/c6cs00551a.
[42] P. Dorenbos, Lanthanide 4f-electron binding energies and the nephelauxetic effect in wide band gap compounds, J. Lumin. 136 (2013) 122–129, https://doi.org/10.1016/j.jlumin.2012.11.030.
[43] T. Karali, P.D. Townsend, M. Prokić, A.P. Rowlands, Comparison of TL spectra of co-doped dosimetric materials, Radiat. Protect. Dosim. 84 (1999) 281–284, https://doi.org/10.1093/oxfordjournals.rpd.a032738.
[44] T. Karali, A.P. Rowlands, M. Prokić, P.D. Townsend, E. Halmagean, Y.S. Horowitz, L. Oster, Thermoluminescent spectra of rare earth doped MgB_4O_7 dosemeters, Radiat. Protect. Dosim. 100 (2002) 333–336, https://doi.org/10.1093/oxfordjournals.rpd.a005882.
[45] N.K. Porwal, R.M. Kadam, T.K. Seshagiri, V. Natarajan, A.R. Dhobale, A.G. Page, EPR and TSL studies on MgB_4O_7 doped with Tm: role of BO_3^{2-} in TSL glow peak at 470 K, Radiat. Meas. 40 (2005) 69–75, https://doi.org/10.1016/j.radmeas.2005.04.007.
[46] N. Salah, S. Habib, S.S. Babkair, S.P. Lochab, V. Chopra, TL response of nanocrystalline MgB_4O_7:Dy irradiated by 3 MeV proton beam, 50 MeV Li^{3+} and 120 MeV Ag^{9+} ion beams, Radiat. Phys. Chem. 86 (2013) 52–58, https://doi.org/10.1016/j.radphyschem.2013.01.034.
[47] C. Furetta, M. Prokić, R. Salamon, G. Kitis, Dosimetric characterisation of a new production of MgB_4O_7:Dy,Na thermoluminescent material, Appl. Radiat. Isot. 52 (2000) 243–250, https://doi.org/10.1016/S0969-8043(99)00124-4.
[48] E.C. Karsu, M. Gökçe, A. Ege, T. Karali, N. Can, M. Prokić, Kinetic characterization of MgB_4O_7:Dy,Na thermoluminescent phosphor Related content, J. Phys. D Appl. Phys. 39 (2006) 1485–1488, https://doi.org/10.1088/0022-3727/39/8/005.
[49] A. Cano, P.R. González, C. Furetta, Further studies of some TL characteristics of MgB_4O_7: Dy, Na phosphor, Mod. Phys. Lett. B 22 (2008) 1997–2006, https://doi.org/10.1142/S0217984908016674.
[50] O. Annalakshmi, M.T. Jose, U. Madhusoodanan, B. Venkatraman, G. Amarendra, Synthesis and thermoluminescence characterization of MgB_4O_7:Gd,Li, Radiat. Meas. 59 (2013) 15–22, https://doi.org/10.1016/j.radmeas.2013.10.001.
[51] E.G. Yukihara, E.D. Milliken, L.C. Oliveira, V.R. Orante-Barrón, L.G. Jacobsohn, M. W. Blair, Systematic development of new thermoluminescence and optically stimulated luminescence materials, J. Lumin. 133 (2013) 203–210, https://doi.org/10.1016/j.jlumin.2011.12.018.
[52] A. Vedda, M. Fasoli, Tunneling recombinations in scintillators, phosphors, and dosimeters, Radiat. Meas. 118 (2018) 86–97, https://doi.org/10.1016/j.radmeas.2018.08.003.
[53] E.G. Yukihara, A.C. Coleman, R.H. Biswas, R. Lambert, F. Herman, G.E. King, Thermoluminescence analysis for particle temperature sensing and thermochronometry: principles and fundamental challenges, Radiat. Meas. 120 (2018) 274–280, https://doi.org/10.1016/j.radmeas.2018.05.007.